

Lcn2 mediates adipocyte-muscle-tumor communication and hypothermia in pancreatic cancer cachexia



Mengistu Lemecha^{1,*}, Jaya Prakash Chalise¹, Yuki Takamuku^{1,2}, Guoxiang Zhang¹, Takahiro Yamakawa¹, Garrett Larson¹, Keiichi Itakura¹

ABSTRACT

Objective: Adipose tissue is the largest endocrine organ. When activated by cancer cells, adipocytes secrete adipocytokines and release fatty acids, which are then transferred to cancer cells and used for structural and biochemical support. How this metabolic symbiosis between cancer cells and adipocytes affects skeletal muscle and thermogenesis during cancer cachexia is unknown. Cancer cachexia is a multiorgan syndrome and how the communication between tissues is established has yet to be determined. We investigated adipose tissue secretory factors and explored their role in crosstalk of adipocytes, muscle, and tumor during pancreatic cancer cachexia.

Methods: We used a pancreatic cancer cachexia mouse model generated by syngenic implantation of pancreatic ductal adenocarcinoma (PDAC) cells (KPC) intraperitoneally into C57BL/6 mice and *Lcn2*-knockout mice. For *in vitro* studies, adipocytes (3T3-L1 and primary adipocytes), cachectic cancer cells (Panc0203), non-cachectic cancer cells (Du145 cells), and skeletal muscle cells (C2C12 myoblasts) were used.

Results: To identify molecules involved in the crosstalk of adipose tissue with muscle and tumors, we treated 3T3-L1 adipocytes with conditioned medium (CM) from cancer cells. Upon screening the secretomes from PDAC-induced adipocytes, several adipocytokines were identified, including lipocalin 2 (*Lcn2*). We investigated *Lcn2* as a potential mediator of cachexia induced by adipocytes in response to PDAC. During tumor progression, mice exhibited a decline in body weight gain, which was accompanied by loss of adipose and muscle tissues. Tumor-harboring mice developed drastic hypothermia because of a dramatic loss of fat in brown adipose tissue (BAT) and suppression of the thermogenesis pathway. We inhibited *Lcn2* with an anti-*Lcn2* antibody neutralization or genomic ablation in mice. *Lcn2* deficiency significantly improved body temperature in tumor-bearing mice, which was supported by the increased expression of *Ucp1* and β 3-adrenergic receptor in BAT. In addition, *Lcn2* inhibition abrogated the loss of fat and muscle in tumor-bearing mice. In contrast to tumor-bearing WT mice, the corresponding *Lcn2*-knockout mice showed reduced ATGL expression in iWAT and decreased the expression of muscle atrophy molecular markers MuRF-1 and Fbx32.

Conclusions: This study showed that *Lcn2* is causally involved in the dysregulation of adipose tissue—muscle-tumor crosstalk during pancreatic cancer cachexia. Therapeutic targets that suppress *Lcn2* may minimize the progression of cachexia.

Published by Elsevier GmbH. This is an open access article under the CC BY-NC-ND license (<http://creativecommons.org/licenses/by-nc-nd/4.0/>).

Keywords Cachexia; Thermogenesis; BAT; *Lcn2*; PDAC; Hypothermia

1. INTRODUCTION

Cancer cachexia is a systemic metabolic dysfunction that affects more than 80% of pancreatic cancer patients and is the leading cause of death in 22%–30% of all cancers [1,2]. Because the cancer spread beyond the pancreas at the time of diagnosis, only about 20% of patients are candidates for surgery [3]. Pancreatic cancer's aggressiveness destabilizes whole-body homeostasis by dismantling the normal network of organs crosstalk. This miscommunication favors the tumor progression during cancer cachexia, which is characterized by devastating body weight loss,

muscle atrophy, fat wasting, decreased appetite [4,5]. The molecular mechanisms underlying these metabolic cues are still being investigated.

Tissues such as the liver, adipose, muscle, and intestine have long been recognized as being important in energy intake and utilization. However, how these organs interact with one another during cancer cachexia is still not clear. One fundamental strategy for coordinating whole-body metabolism is communication between tissues via secreted factors [6]. In fact, the role of adipose tissue in organ crosstalk has been extensively studied [7], particularly during insulin resistance [8]. However, little is known about adipose tissue

¹Department of Molecular and Cellular Biology, Beckman Research Institute of City of Hope, Duarte, CA, USA ²Department of Central Research Institute, Wakunaga Pharmaceutical Co., Ltd., Akitakata, Hiroshima, Japan

*Corresponding author. Department of Molecular and Cellular Biology, Beckman Research Institute of City of Hope 1500 E Duarte Rd, Duarte, CA 91010, USA. E-mail: mshukare@coh.org (M. Lemecha).

Received July 26, 2022 • Revision received September 22, 2022 • Accepted October 10, 2022 • Available online 13 October 2022

<https://doi.org/10.1016/j.molmet.2022.101612>

remodeling and the role of its secreted factors during pancreatic cancer induced cachexia.

Aside from energy mobilization, adipose tissue is one of the largest endocrine organs, accounting for 20–25% of total body mass. Adipocytes secrete multiple hormones and cytokines known as adipokines or adipocytokines, which are key in inter- and intra-organ communication [9]. The communication between cancer cells and adipocytes is initiated by cancer-derived inflammatory mediators. These tumor factors stimulate adipocytes to produce adipokines, such as TNF- α , IL-6, and MCP-1; these adipokines have been linked to tumor progression and cancer cachexia-induced atrophy [10]. However, the precise adipocytokines that mediate the interaction of adipose tissue with tumor have not been identified.

The energy demand of cancer cells triggers lipolysis, which is the breakdown of triacylglycerol into free fatty acids and glycerol [11]. Lipolysis results in elevated flux of fatty acids into the skeletal muscle. Excessive fatty acid oxidation in the muscle leads to muscle atrophy [12]. Lipolysis inhibition by deletion of adipose triglyceride lipase alleviated muscle wasting in cachectic mice. Furthermore, inhibition of fatty acid oxidation pharmacologically rescued human myotube atrophy and increased muscle mass [12,13,58]. While lipolysis normally triggers thermogenesis in brown adipose tissue (BAT) and browning of white adipose tissue (WAT), cancer impairs this process and causes hypothermia, in which more heat is lost than generated [14,15]. However, BAT contribution to hypothermia and its influence on thermogenesis pathways during pancreatic cancer cachexia is unclear.

We hypothesized that adipocytes may play key roles in bridging tumor and systemic metabolism through a mechanism involving the adipocyte secretome. In this regard, we investigated the adipocytokines involved in the communication between adipose tissue with tumor and muscle. We identified *Lcn2* *in vitro* and investigated its function using a cachectic mouse model of pancreatic ductal adenocarcinoma (PDAC). We found that inhibition of *Lcn2* alleviated the suppression of the thermogenesis in the BAT of pancreatic cancer cachexia mice.

2. MATERIALS AND METHODS

2.1. Animals and experimental design

Male C57BL/6 mice and *Lcn2*-knockout (KO) mice (#024630) were obtained from Jackson Laboratory (Jackson Labs, Bar Harbor, ME, USA) [16]. The pancreatic cancer cachexia model mice were generated following a previously established protocol [17]. Briefly, after one week of acclimatization, either KPC cells (5×10^6 cells in 0.2 ml saline) or PBC were injected intraperitoneally. KPC cells (KPCY, a mouse pancreatic cancer cell line) were obtained from Kerastat Inc (Boston, MA, USA). Food intake and body weight were recorded. Mice were randomly assigned to groups on the basis of body weight on the day of tumor cell inoculation.

All experiments with mice were reviewed and approved by the City of Hope Institutional Animal Care and Use Committee (#20039). Mice were maintained in a 12-h dark/light cycle and housed in groups of three to five mice with unlimited access to water and food (standard chow diet #5058, LabDiet, St. Louis, MO, USA).

2.2. Tissue collection

Mice were euthanized with isoflurane inhalation and inguinal WAT (iWAT), epididymal WAT (eWAT), interscapular BAT, gastrocnemius muscle, soleus muscle, tibialis anterior muscle, liver, spleen and pancreas were dissected immediately. Tissues were snap frozen in

liquid nitrogen and stored at -80°C until analysis, except for histological analysis.

2.3. Body temperature measurements

Body surface temperature was recorded with an infrared camera (Compact-Infrared-Thermal-Imaging Camera E60bx, FLIR, West Malling, Kent, UK). Briefly, the infrared thermometer sensor temperature was used to capture temperature from the lower abdomen of mice, with the outer flat surface of the thermometer held approximately 2–5 mm away from the surface of the abdomen [18,19].

2.4. Blood analysis

Blood glucose levels were measured using whole blood taken from the tail vein using a glucometer (Clarity Diagnostics, Boca Raton, FL, USA). For other analyses, blood samples were collected from the tail vein with a heparinized tube and centrifuged at $700 \times g$ for 15 min. Plasma samples were stored at -80°C until further analysis. Plasma levels of lipocalin 2 were determined using the mouse lipocalin 2 ELISA kit (Thermo Fisher Scientific, Waltham, MA, USA).

2.5. Histology

For hematoxylin and eosin (H&E) staining, tissues were harvested and fixed immediately in 10% neutral buffered formalin. Dehydration, clear and paraffinization were performed on a Tissue-Tek VIP Vacuum Infiltration Processor (Sakura). The samples were embedded in paraffin using a Tissue-Tek TEC Tissue Embedding Station (Sakura) and sectioned at $5 \mu\text{m}$; the sections were placed on positively charged glass slides. The slides were deparaffinized, rehydrated and stained with Modified Mayer's Hematoxylin and Eosin Y Stain (America MasterTech Scientific) on a H&E Auto Stainer (Prisma Plus Auto Stainer, Sakura) following standard laboratory procedures.

For Masson's trichrome staining, staining was conducted using the Eprelia™ Richard-Allen Scientific Masson Trichrome Kit (Thermo Fisher Scientific). Briefly, after deparaffinization and rehydration, the slides were immersed in Bouin's solution at 60°C for 1 h. The slides were washed and stained in Weigert's hematoxylin. Next, the slides were stained in Biebrich scarlet-acid fuchsin and incubated in phosphotungstic-phosphomolybdic acid after staining with aniline blue. The slides were then rinsed, dehydrated and mounted. After H&E or trichrome staining, whole slide images were acquired with a Ventana iScan HT Scanner (Roche) and viewed by iScan image viewer software.

2.6. Immunofluorescence and immunohistochemistry staining

Paraffin-embedded sections were deparaffinized and incubated for 30 min with 0.3% H_2O_2 in methanol to block endogenous peroxidase. Endogenous avidin and biotin were blocked using the Histo blocking kit (Nacalai, Kyoto, Japan), as described previously [20]. Detail procedures for immunofluorescent and immunohistochemistry are provided in supplementary file.

Fusion index (% nuclei within MyHC-positive myotubes) was calculated as the number of nuclei inside myotubes with two or more nuclei as a percentage of the total number of nuclei. Nuclei were quantified using MyoCount (automated quantification of myotube surface area and nuclear fusion index) [67,68].

2.7. MitoTracker and BODIPY staining

MitoTracker Red CMXRos (Invitrogen Molecular Probes, Inc., Eugene, OR, USA), a mitochondria-specific cationic fluorescent dye, was used to label mitochondria. BODIPY lipid labeling 493/503, Invitrogen (Life

Technologies, Eugene, OR, USA) was used to stain for lipids. For staining, 3T3-L1 cells grown on BD Flacon culture slides were incubated with 250 nmol/L MitoTracker or 4 μ M BODIPY in serum-free DMEM for 15 min at 37 °C following the manufacturers' instructions. Images were visualized using a Zeiss LS700 confocal laser scanning microscope.

2.8. Western blotting

Proteins were separated by SDS-PAGE using Criterion™ TGX™ pre-cast gels (Bio-Rad) and transferred to PVDF membranes (Bio-Rad) using the Trans-Blot Turbo System (Bio-Rad). Immunoblotting was performed using the following primary antibodies diluted in 5% milk: monoclonal mouse anti-MyHC (1:1000; MAB4470, Clone #MF20), rat anti-mouse Lipocalin-2/NGAL (1:1000, Catalog #MAB1857) from R&D Systems, Minneapolis, MN, USA; rabbit anti-vinculin (1:1000; #13901), mouse anti-adipose triglyceride lipase (ATGL) (1:1000; #2138), rabbit anti-cleaved caspase 3 (1:1000; #9664S), rabbit anti-hormone sensitive lipase (HSL; 1:2000; # 4107S), anti-phospho HSL (Ser660; 1:1000; # 4126S) from Cell Signaling Technology, Beverly, MA, USA; mouse anti-pyruvate dehydrogenase (1:3000; Novus Biologicals, Cambridge, UK); mouse anti-GAPDH (1:500; AM4300, Invitrogen, Rockford, IL, USA); and mouse anti-cytochrome c (1:1000, #338500, Life Technologies, Rockford, IL, USA). We used the following secondary antibodies diluted at 1:1000 in 5% milk: goat anti-mouse IgG-HRP (31430), goat anti-rabbit IgG-HRP (31460) (both from Invitrogen), and anti-rat (HAF005; R&D, Minneapolis, MN, USA). Protein bands were visualized using ECL select detection reagent (Amersham, Little Chalfont, UK). The protein band intensities (densitometry) were quantified using Image J software.

2.9. Flow cytometry

The iWAT or BAT fat pad was dissected, and cells isolated as previously described [21]. Briefly, tissues were minced and digested with 1.5 U/ml collagenase D (Roche, Mannheim, Germany) in 10 mM CaCl₂ and 2.4 U/ml dispase II (Roche) for 40–50 min while shaking at 37 °C. Digestion was stopped by adding complete DMEM/F12 containing 10% FCS and penicillin/streptomycin (SV culture medium). Cells were collected by centrifugation at 300 \times g for 5 min, resuspended and filtered through a 70 μ m cell strainer (Falcon). Next, cells were stained with FC block CD16/32 (Clone 93, Biolegend San Diego, cat no: 101302) followed by staining with FACS antibodies specific to macrophages and T lymphocytes following the manufacturer instructions. Antibodies used for FACS staining were APC/Cy7 anti-mouse CD45 (Clone 30-F11), PE anti-mouse F4/80 (clone BM8), APC anti-mouse CD11b (clone M1/70), FITC-anti-mouse CD206 (clone C068C2) and PE/Cy7 anti-mouse CD4 (clone GK1.5). All antibodies were obtained from Biolegend (San Diego, CA, USA). The stained cells were analyzed by BD Fortessa and the acquired data were analyzed by FCS Express 7 research edition.

2.10. Measurement of body composition and metabolic parameters

Body composition and comprehensive metabolic phenotyping were measured as described previously [22]. Briefly, whole body composition (fat and lean tissues) was determined using quantitative magnetic resonance technology (EchoMRI™ 3-in-1; Echo Medical Systems, Houston, TX, USA). Automatic tuning and calibration of the instrument parameters using canola oil maintained at room temperature (22 °C) were performed daily. Individual mouse was placed in the analytical chamber. Parameters measured by the EchoMRI™ included lean mass (g), fat mass (g), free water (g) and total water (g). An

indirect calorimetry cage system (Promethion, Sable Systems, Las Vegas, NV, USA) was used to measure oxygen consumption (VO₂), CO₂ production (VCO₂), respiratory quotient (RQ), energy expenditure, food intake, water consumption, locomotor activity and animal weight. The Promethion is an indirect calorimetry system with gas sensing units used to measure VO₂ and VCO₂. The cages also contained high precision sensor—associated-feeding baskets to accurately measure food intake (g), with a meal defined as intake over 0.01 g. A multi-dimensional infrared beam system allowed the measurement of locomotor activity, which was defined as the total number of infrared beam breaks in the X and Y axis. The software captures metabolic parameters in each cage every 5 min. Mice were weighed and then individually housed in cages for 4 days. Animals were acclimated to the cages for 1 day and experimental data were collected for 72 h following the acclimation day. Animals were given *ad libitum* access to food and water for the duration of the experiment. The light cycle was from 6:00 to 18:00 h. Animals were observed daily, and animal weight was obtained at the conclusion of the experiment. Data were analyzed using CalR (a web-based analysis tool) [23].

2.11. Cell culture and conditioned media preparation

C2C12 (a mouse myoblast skeletal muscle cells), Panc0203 (a human pancreatic adenocarcinoma cell line) and Du145 (a human prostate cancer cell line) were obtained from the ATCC (Manassas, VA, USA). KPC cells (KPCY, a mouse pancreatic cancer cell line) were obtained from Kerafast Inc (Boston, MA, USA). All cells were grown in Dulbecco's modified Eagle's medium (DMEM) supplemented with 10% (v/v) fetal bovine serum (FBS), 100 units/mL penicillin and 100 mg/mL streptomycin in a humidified atmosphere of 95% air and 5% CO₂ at 37 °C.

C2C12 myoblasts were differentiated as previously reported [24] with little modification. Briefly, C2C12 cells were grown to near confluence (90%) before the induction and transferred to DMEM containing 2% horse serum (Gibco) (HCM). For recombinant Lcn2 treatment, C2C12 cells were treated with 1 μ g per ml of Lcn2 (#SRP6537, Sigma) from day 4–6 post induction. The 3T3-L1 pre-adipocyte cell line was cultured as previously reported [21]. Briefly, 3T3-L1 cells were maintained in growth medium containing DMEM (25 mM glucose) supplemented with 10% FBS at 37 °C in 10% CO₂ until confluent. Two days after the cells reached full confluency, 3T3-L1 cells were induced to differentiate by replacing the media with induction media containing 10% FBS and differentiation inducers (0.5 mM 3-isobutyl-1-methylxanthine, 0.25 μ M dexamethasone and 10 μ g/ml insulin). After two days, the medium was replaced with adipocyte-maintained media (ADM) containing 10% FBS and DMEM.

To prepare cancer adipogenic conditioned medium (CADM), cancer conditioned media (CCM) was first prepared from cancer cells (Panc0203, Du145 and KPC) by collecting 48 h after cultured cells reached 90% confluency. Non-conditioned media (NCM) was prepared similarly by incubating cancer cells growth media without cells. The CCM and NCM were filtered and stored at –80 °C.

To obtain cancer induced adipocyte differentiation media (CIADM), CCM was diluted with ADM at a 1:3 ratio. Adipocytes were treated with either ADM or CIADM from day 6–12 and media were replaced every other day. On day 12, cancer adipogenic media (panc0203-adipo; Du145-adipo) and NCM-adipogenic media (NCM-adipo) were collected, filtered, and stored at –80 °C.

For myotube development studies, HCM was diluted with different conditioned media (NCM, NCM-adipo, Panc0203-adipo or KPC-adipo) at a 1:3 ratio and C2C12 cells were treated from day 2–6 post induction.

2.12. Primary adipocyte differentiation from stromal vascular culture and conditioned media preparation

The iWAT fat pad (eight fat pads) was dissected from 8-week-old C57BL/6 mice. The primary stromal-vascular fraction (SVF) was differentiated into beige adipocytes, as previously described [21]. Detail procedure is provided in supplementary file.

2.13. ELISA

To measure Lcn2 in cell culture media and plasma, the Lipocalin-2 (Lcn2) Mouse ELISA Kit was used following the manufacturer's instructions (Invitrogen, EMLCN2, Frederick, MD, USA).

2.14. Protein array

Conditioned media collected from adipocytes were subjected to immunoblotting-based protein profiling using the Proteome Profiler Mouse XL Cytokine Array kit (ARY028; R&D Systems, Minneapolis, MN, USA) following the manufacturer's instructions. Briefly, conditioned media from adipocytes was collected after treatment with conditioned media from cancer cells or non-conditioned media for 48 h. Total protein concentration was determined using the Pierce BCA Protein Assay Kit (Thermo Fisher Scientific), and protein concentration was normalized across the samples. Membrane images were developed with the Bio-Rad ChemiDoc MP imaging system. The protein band intensities were quantified by HLIimage++ image processing software (Western Vision Software, Salt Lake City, UT, USA).

2.15. Antibody neutralization

The neutralizing monoclonal antibodies targeting mouse Lipocalin-2/NGAL MAb (#MAB1857-MTO, clone 228418) or IgG control (rat IgG2A Isotype #MAB006-MTO, clone 54447) were obtained from R&D Systems (Minneapolis, MN, USA). One hundred micrograms per mouse were administered via intraperitoneal injection twice weekly for 3 weeks.

2.16. Glycerol, fatty acid and lactate dehydrogenase assay

Glycerol was quantified using the Sigma–Aldrich glycerol assay kit colorimetric assay following the manufacturer's instructions. Samples were diluted using sterile water to a detectible concentration within the standard curve. The free fatty acid concentration was measured using a NEFA-HR (2) kit Wako (FUJIFILM Wako Pure Chemical Corporation, Osaka, Japan) following the manufacturer's instructions. Lactate dehydrogenase (LDH) in the conditioned media was measured using the LDH assay kit (ab102526, abcam) following the manufacturer's instructions.

2.17. Quantitative real-time PCR (qRT-PCR)

The qPCR reaction setup and plate preparation were standardized and carried out following standard operating protocols as described previously [25]. Briefly, single-stranded cDNA was synthesized from 0.75 µg of total RNA using the iScript cDNA Synthesis Kit (Bio-Rad, Hercules, CA, USA) and endogenous genomic DNA was degraded using the RNase-free DNase set (Qiagen). Experimental transcript levels were analyzed using iQTM SYBR Green Supermix (Bio-Rad) using the CFX96™ Real-Time System. Non-template control (NTC) was used as a negative control. The amplification efficiency for each primer pair was calculated by standard curve methods. A Ct value > 35 was considered below the detection limit in our study. qRT-PCR data were normalized to Ribosomal Protein L13a (*RPL13a*) mRNA expression. Thermal cycling conditions were 95 °C for 3min, followed by 40 cycles of 95 °C for 10 s and 58 °C for 30 s. Primer sequences are listed in [Supplementary Table 2](#).

2.18. RNA isolation, RNA-seq sequencing library preparation and RNA sequencing

Total RNA isolation from BAT was performed using the RNeasy kit (Qiagen, Germany). RNA quality was determined with an Agilent Bioanalyzer RNA NanoChip (RNA integrity number [RIN] > 8 for all samples). RNA sequencing libraries were prepared with the Kapa mRNA HyperPrep kit (Kapa Biosystems, Cat KR1352) following the manufacturer's protocol. The final libraries were validated with the Agilent Bioanalyzer DNA High Sensitivity Kit and quantified with Qubit. The libraries were sequenced on the NovaSeq 6000 platform with S4 reagent kit v1.5 (200 cycles) with paired end mode of 2 × 101. Real-Time Analysis (RTA) v3.4.4 software was used for base calling and Illumina bcl2fastq v2.20.0.422 to convert base call (BCL) files into FASTQ files.

2.19. RNA sequencing analysis

RNA sequencing reads were trimmed to remove sequencing adapters using Trimmomatic [26] and polyA tails using FASTP [27]. The trimmed reads were mapped against the mm10 mouse reference genome using STAR version 2.7.9 [28]. Read counts mapped to genes were measured by feature Counts in R package "Rsubread" version 2.8.2 [29]. A total of 21,837 coding genes were analyzed for transcript abundance and 12,716 out of 21,837 poorly expressed genes were removed using the criteria of RPKM >1 for at least two samples. Remaining read counts were normalized using the Trimmed Mean of M-values normalization method. Differentially expressed genes were identified using the R package "edgeR" version 3.36.0 [30]. The fold change and P values were calculated using glmQLFTest in "edgeR." Fold changes ≥1.5 and FDR <0.05 were used to identify the significant gene expression changes. The identified differentially expressed genes were used to generate a heatmap using Cluster 3.0 and Treeview [31].

2.20. Gene ontology and pathway enrichment analyses

Hierarchical clustering and principal component analysis (PCA), gene set enrichment and pathway analysis (GSEA) for enriched Gene Ontology (GO) terms and KEGG pathways were performed using the parametric gene set enrichment analysis (PGSEA) by IDEPv905 (integrated Differential Expression and Pathway analysis [32–35,66]. Volcano plot analysis was conducted using ShinyGO v0.76 tool [36].

2.21. Statistical analyses

Results are expressed as mean ± SEM. Student's t test was used to evaluate differences between two groups. One-way ANOVA and a subsequent post hoc Tukey test were used to determine the significance of differences where multiple comparisons were required. $P < 0.05$ was considered statistically significant.

3. RESULTS

3.1. Adipocyte secretome induced by PDAC reduced skeletal muscle myogenesis, and Lcn2 was identified as a possible mediator

To explore the communication between adipocytes with cancer and muscle cells *in vitro*, we used cancer cells pancreatic cancer Panc0203 and prostate cancer Du145 cells, adipocytes (3T3-L1) and skeletal muscle cells (C2C12) ([Supplementary Fig. 1B](#)). Panc0203 cells were used as cachectic cancer cells, whereas Du145 cells were used as non-cachectic cancer cells.

To explore whether cachectic cells might influence lipolysis in adipocytes, we collected CM from cancer cells and treated 3T3-L1 adipocytes with conditioned medium (CM) from cancer cells on days 6–12

of adipocyte differentiation. Oil red O staining revealed reduced lipid accumulation in adipocytes treated with CM derived from Panc0203 cells in comparison with non-conditioned media (NCM, control 1) or the CM of Du145 cells (control 2) (Figure 1A). Immunofluorescent labeling with BODIPY (for lipid) and Mitotracker (for mitochondria) demonstrated decreased lipid accumulation and lower mitochondrial mass in cells treated with CM from Panc0203 cells (Figure 1B). The levels of both free fatty acid and glycerol in the CM from adipocytes treated with CM from Panc0203 cells were significantly higher compared with controls ($p < 0.05$) (Figure 1C). This was supported by significantly higher expression of hormone sensitive lipase (*HSL*) (Figure 1C), along with increased levels of phosphorylated HSL (Supplementary Fig. 1A). Together these results indicate an increase in lipolysis in adipocytes treated with CM from Panc0203 cells.

To test the effect of cancer adipogenic media on myotube development, C2C12 cells were cultured with either Panc0203 adipogenic media (Figure 1D–E) or Panc0203 CM (Supplementary Figs. 1E–F). The expression of myosin heavy chain (MyHC) was markedly reduced in Panc0203 adipogenic media compared with controls (Figure 1D). In addition, immunofluorescence staining for MyHC showed that Panc0203 adipogenic media reduced myotube diameter with significantly a lower fusion index (Figure 1E) and increased expression of *Fbx32* (Supplementary Fig. 1H). These findings suggest that inhibition of myotube development *in vitro* faithfully models cachexia phenotype. Next, we sought to identify the molecular factors released by adipocytes. The secretomes of adipocytes treated with CM derived from Panc0203 or Du145 cells were compared with that of untreated CM of 3T3-L1 adipocytes using protein arrays. Several inflammatory cytokines, including Lipocalin 2 (*Lcn2*), CXCL1, CXCL5, and Osteopontin, were robustly increased in the PDAC-induced adipocyte secretomes in comparison with the non-cachectic controls (Figure 1F–G).

For the subsequent investigation, we selected *Lcn2*, because of the following reasons. 1) *Lcn2* was previously identified as an adipocytokine and characterized as an important regulator of inflammation [37,38], and 2) MyHC expression and myotube diameter were substantially reduced in C2C12 cells with recombinant *Lcn2* treatment (Figure 1K–L).

To confirm the protein array results, we carried out immunoblotting and ELISA assays. *Lcn2* protein expression (Figure 1H) and secretion (Figure 1I) were dramatically increased in adipocytes treated with PDAC cell CM. In addition, mRNA expression of *Lcn2* was increased by more than hundreds fold when adipocytes are treated with Panc0203 CM (Figure 1J) indicating stimulation of *Lcn2* in adipocytes. The *in vitro* models treated with conditioned media did not exhibit apoptosis as shown by absence of caspase 3 cleavage and no change in lactate dehydrogenase (LDH) activity (Supplementary fig. 1C, D and G). To examine the effect of *Lcn2* on skeletal muscle cells, we treated C2C12 cells with recombinant *Lcn2*. MyHC expression and myotube diameter were substantially reduced with *Lcn2* treatment (Figure 1K–L).

3.2. Thermogenesis was suppressed in BAT during PDAC-induced cachexia

We further explored adipose tissue remodeling by generating a PDAC-induced cachectic mouse model as previously reported [17] and described in the methods section. We implanted KPC tumor cells intraperitoneally into C57BL/6 mice (KPCi group) and used phosphate-buffered saline (PBS) as a control (PBS group) (Figure 2A). The plasma level of *Lcn2* in KPCi mice increased by more than 3-fold at day 8 post tumor cell implantation compared with that in the control groups ($p = 0.0003$) (Figure 2B). In addition, *Lcn2* protein expression was dramatically increased in the iWAT of KPCi mice (Figure 2C). The KPCi

mice began to lose weight on day 10 (Supplementary Fig. 2A). A significant decrease in the weight of epididymal adipose tissue (eWAT) ($p < 0.01$), inguinal white adipose tissue (iWAT) ($p < 0.01$), brown adipose tissue (BAT) ($p < 0.01$), tibialis anterior (TA) and gastrocnemius muscle ($p < 0.05$) were observed in KPCi mice compared with controls. In contrast, the tissue weight of spleen and pancreas ($p < 0.05$) was increased compared with the control group (Supplementary Fig. 2B). Furthermore, wasting in total body fat depots was observed in KPCi mice beginning on day 4 as measured by MRI (Supplementary Fig. 2C), despite no change in lean mass (Supplementary Fig. 2D). These results confirm the phenotype of pancreatic cancer-induced cachexia. The KPCi mice also exhibited a significant increase in non-fasting blood glucose level ($p < 0.05$) (Supplementary Fig. 2E).

The dramatic loss of BAT promoted us to examine the normothermic phenotype of the cachectic mice. Adipose tissue, BAT in particular, controls the body temperature by non-shivering thermogenesis [39–41]. Therefore, we measured the body temperature during tumor progression. At day 12, the KPCi mice had a considerably lower body temperature compared with the control ($p < 0.05$) (Figure 2D). The gross histologic image of BAT demonstrated complete fat consumption in the KPCi mice compared with the controls (Figure 2E). To evaluate the time course of fat utilization, hematoxylin and eosin (Figure 2F) and oil red O (Figure 2G) staining of BAT was carried out at days 4 and 10. While there was no difference in fat depots between groups at day 4, a markedly reduction of fat depots in the KPCi group compared with control mice was observed at day 10.

We observed the appearance of a considerable number of nuclei in BAT of KPCi mice isolated on day 10. Therefore, we performed FACS analyses on cells isolated from BAT on days 4 and 10 after tumor inoculation. Unexpectedly, we observed no difference in total immune cells CD45+ and CD11b + F4/80+ cells between groups on day 10 (Figure 2H–I), implying that the increase in nuclei (Figure 2F) may be from an increase in adipocytes occupying the same space because of severe fat loss. In contrast, we noticed a significant increase in immune cells in BAT extracted from tumor-bearing mice on day 4, showing that BAT inflammation occurs at the early stage of tumor growth ($p < 0.05$) (Figure 2H–I). Together, these results suggests that the observed hypothermia may be mediated by BAT dysfunction.

To identify the pathways and changes of the gene profiles in BAT in response to tumor progression, we isolated RNA from BAT of KPCi and control mice, performed RNA-seq analysis and mapped the transcriptional changes (Supplementary Table 1). The results identified 2059 differentially expressed genes in the KPCi mice, including 1057 increased and 1002 decreased genes. Heatmap analysis revealed that genes differentially expressed between the KPCi and control groups were clearly distinct (Supplementary Fig. 2F). The principal component analysis plot showed distinguished clusters of genes from BAT of KPCi and control mice (Supplementary Fig. 2G).

We identified top ranking pathways by running PGSEA on Kyoto Encyclopedia of Genes and Genomes (KEGG) using IDEPv905 (Figure 2J). Thermogenesis was one of the top metabolic pathways that is significantly suppressed during tumor progression. RNAseq analysis also revealed that *Lcn2* was one of the most highly expressed genes in BAT from KPCi mice (Figure 2K). Hypothermia is induced when thermogenesis is decreased, which is related to decreased mitochondrial content and metabolic rate [42]. Notably, we found a significant decrease of beta-adrenergic receptor (*Adrb3*), protein kinase A (*Prkaa1*) and peroxisome proliferator-activated receptor-gamma coactivator-1 alpha (*Ppargc-1α*) expression in BAT, all of which are key regulators of mitochondrial biogenesis (Figure 2L,

Figure 1

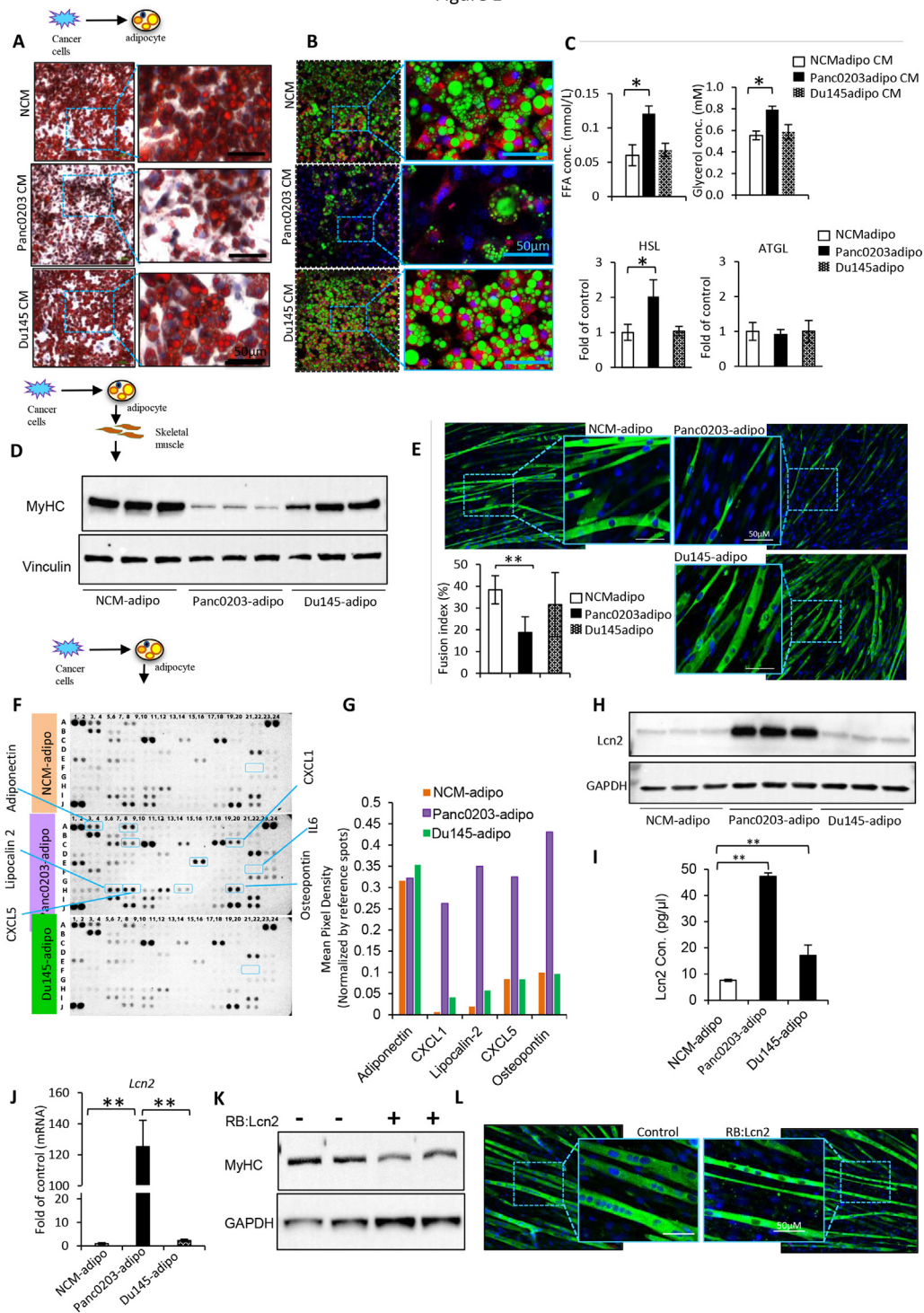


Figure 1: PDAC-induced adipocyte secretome inhibited myotube development and Lcn2 was identified as a potential mediator. **A)** Oil Red O staining of 3T3-L1 adipocytes treated with conditioned media (CM) from cancer cells or non-conditioned media (NCM). **B)** Immunofluorescent staining of perilipin (green) and Mitotracker (red) in 3T3-L1 adipocytes treated with CM from cancer cells or NCM. **C)** Upper panel: glycerol and free fatty acid (FFA) levels were measured in CM collected from adipocytes pre-treated with cancer cell CM, n = 4. Lower panel: qRT-PCR of *HSL* and *ATGL* in adipocytes, n = 5. **D)** Immunoblot analysis of MyHC protein in C2C12 myotubes after treatment with cancer cell-induced adipogenic media, n = 3. **E)** Immunofluorescent staining of MyHC (green) and nuclei (DAPI, blue) in C2C12 cells treated with cancer adipogenic media, n = 4. Fusion index was calculated as the ratio of the nuclei number in myocytes with two or more nuclei versus the total number of nuclei, n = 4. **F)** Protein array detected with immunoblotting from conditioned media of matured 3T3-L1 adipocytes treated with the indicated cancer cell CM. **G)** Densitometric analysis of selected proteins detected in (K). **H)** Immunoblot analysis of Lcn2 in 3T3-L1 matured adipocytes treated with media from cancer cells or non-conditioned media from day 6–12 during adipocyte differentiation, n = 3. **I)** Lcn2 levels in cancer cell-induced adipogenic media measured by ELISA, n = 4. **J)** qRT-PCR of *Lcn2* in adipocytes, n = 5. **K)** Immunoblot analysis of MyHC in C2C12 cells treated with 1 µg/ml of recombinant Lcn2 or DMSO (control) from day 4–6 after induction, n = 4. **L)** Immunofluorescent staining for MyHC (green) and nuclei (DAPI, blue) in C2C12 myotubes treated with 1 µg/ml of recombinant Lcn2 or DMSO (control) from day 4–6 after induction. *p < 0.05, **p < 0.01.

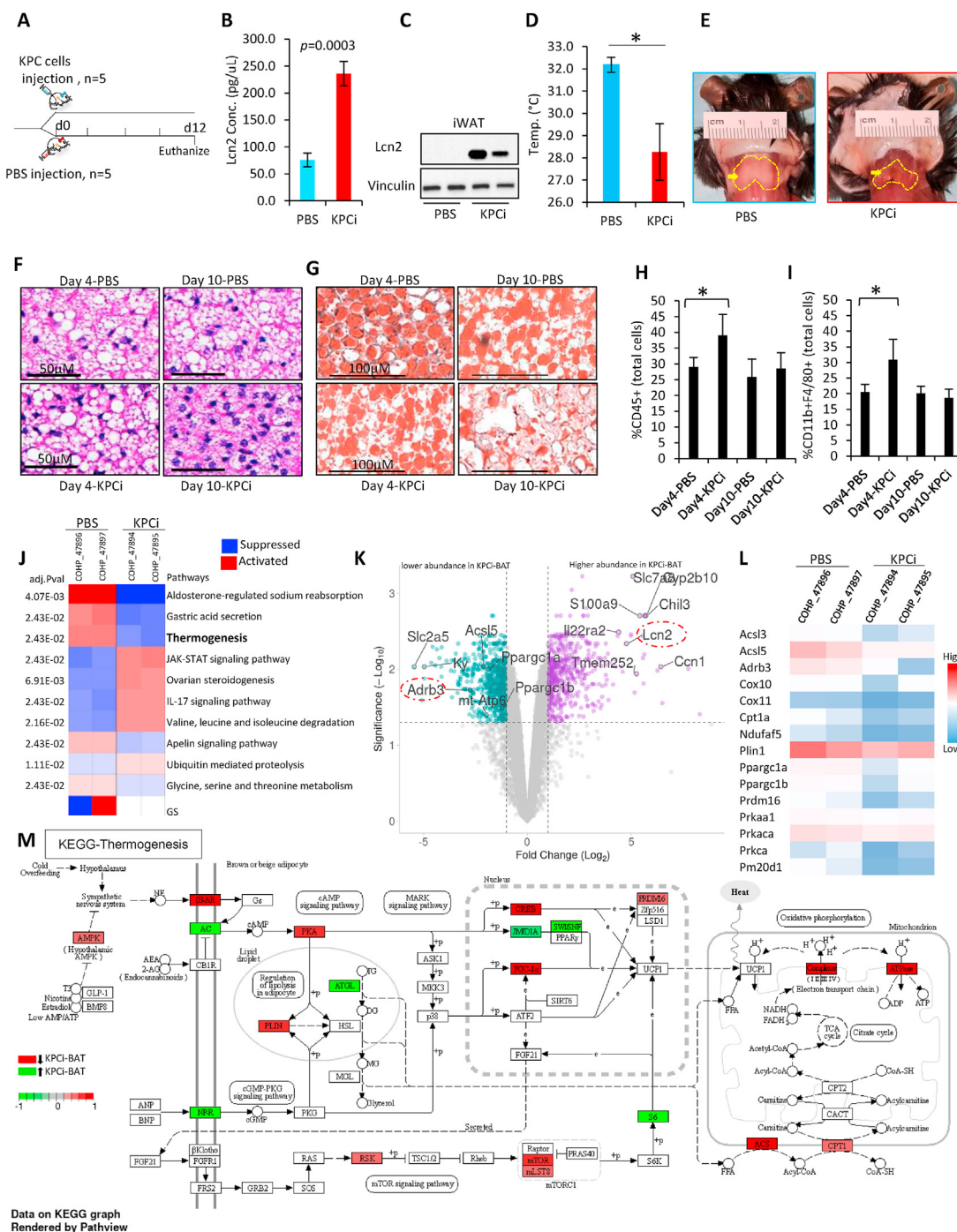


Figure 2: PDAC induced fat loss triggered hypothermia: **A)** Study design. KPC tumor cells (5×10^6) were implanted intraperitoneally into C57BL/6 mice (KPCi group, $n = 5$). The control mice were administered with PBS solution (PBS group, $n = 5$). **B)** Plasma levels of Lcn2 at day 8 post KPC tumor cell implantation or PBS administration in mice were measured by ELISA, $n = 5$. **C)** Immunoblot analysis of Lcn2 in inguinal white adipose tissue (iWAT) from control and KPCi mice, $n = 5$. **D)** Surface body temperature was measured using infrared camera at indicated time points, $n = 5$. **E)** Representative images of gross appearance of brown adipose tissue (BAT) (indicated by yellow dots) from control and KPCi mice are shown. **F, G)** Representative images of hematoxylin and eosin (H&E) (F) and Oil Red O (G) staining of BAT from day 4 and day 10 post KPC tumor cell implantation or PBS administration are shown. **H, I)** FACS analyses were used to identify immune cell populations gated out of total live cells isolated from BAT tissue on day 4 and day 10 post tumor cell implantation of indicated groups of mice. CD45⁺ cells (H) and CD11b + F4/80 + cells (I), $n = 5$. **J)** Top-ranking pathways identified by PGSEA on Kyoto Encyclopedia of Genes and Genomes (KEGG) using IDEPv905. Significance cutoff of FDR < 0.5 and differential pathways are listed according to adjusted p value. Pathways activated are shown in red, and suppressed pathways are shown in blue. **K)** Volcano plot of gene expression of up-regulated (purple) and down-regulated (green) genes in BAT from KPCi mice compared with WT mice using ShinyGo 0.76. Selected genes are indicated. **L)** Heatmap of relative expression of selected thermogenesis-associated genes from the RNA-seq dataset. Genes with $p < 0.05$ are displayed. **M)** Thermogenesis pathway from KEGG. Genes significantly downregulated (red) and upregulated (green) in BAT during tumor progression compared with BAT of control group. * $p < 0.05$, ** $p < 0.01$. For J–M: $n = 2$, gene set downregulated in KPCi mice by > 1.5 fold, FDR < 0.05, $p < 0.05$ compared with WT mice used for analysis.

Supplementary Table 1). In addition, the KEGG results showed downregulation of common thermogenesis-related pathways such as PKA signaling, PPAR signaling, oxidative phosphorylation and the TCA cycle in BAT in KPCi mice (Figure 2M). These findings suggest that pancreatic cancer cachexia induces suppression of thermogenic gene expression in BAT, thereby contributing to the development of hypothermia.

These data suggest that BAT plays a significant role in advancing cachexia during tumor progression.

3.3. Fat wasting in BAT is partly reversed in KPC tumor cell–implanted *Lcn2*-KO mice, thereby improving normothermia

We next examined the interplay of *Lcn2* in the KPC mouse model of pancreatic cancer cachexia. To suppress the expression of *Lcn2*, we injected antibody against *Lcn2* into KPCi mice with IgG as a control (Supplementary Fig. 3A). The administration of an *Lcn2* antibody was able to counteract the increased *Lcn2* level to less than half (Supplementary Fig. 3B), lower non-fasting blood glucose levels (Supplementary Fig. 3E) and maintain body temperature (Supplementary Fig. 3F). However, there was no difference in tissue weight except the spleen (Supplementary Figs. 3C–D). This could be in part because of the inability of the *Lcn2* antibody to suppress *Lcn2* in the circulation to the basal level.

To better delineate the effects of *Lcn2* on cachexia, we used a *Lcn2* null (KO) mouse model. We generated four groups of mice: KO^{*LCN2*}-KPCi (*Lcn2* KO mice implanted with KPC tumor cells), WT-KPCi (wild-type mice implanted with KPC tumor cells), KO^{*LCN2*} (*Lcn2* KO mice injected with PBS) and WT (wild-type mice injected with PBS) (Figure 3A). *Lcn2* levels in plasma were undetectable in the KO mice on day 0 prior to KPC inoculation, confirming the complete knock-out of the *Lcn2* gene. The levels of *Lcn2* in WT-KPCi mice were increased to more than 3-fold higher at day 12 ($p = 2.09E-09$) compared with day 0 (Figure 3B). However, inoculation of KPC into KO^{*LCN2*} mice did not increase *Lcn2*, indicating that tumor derived *Lcn2* secretion is minimal. The body weight loss on day 12 in KPCi mice during tumor progression was significantly reduced by suppression of *Lcn2* in KO^{*LCN2*}-KPCi mice ($p < 0.05$) (Figure 3C).

To examine the tissues that were affected by KO of *Lcn2*, we measured the weights of various tissues. The weight of iWAT, which was reduced in WT-KPCi mice, significantly recovered in KO^{*LCN2*}-KPCi mice (Figure 3D–E). Interestingly, the lack of *Lcn2* increased the skeletal muscle weight of tibialis anterior and gastrocnemius in KO^{*LCN2*}-KPCi mice compared with WT-KPCi mice (Figure 3D–E). Furthermore, non-fasting blood glucose levels in KO^{*LCN2*}-KPCi mice were reduced to levels comparable to those in non-tumor bearing KO^{*LCN2*} or WT mice ($p < 0.05$) (Figure 3F). Importantly, *Lcn2* deficiency partly enabled mice to maintain a higher body temperature compared with WT-KPCi mice ($p < 0.05$) (Figure 3G).

BAT is the primary organ responsible for heat generation via thermogenesis, and therefore we next examined BAT by histological investigation. The gross appearance showed more whitening of the BAT of the KO^{*LCN2*}-KPCi mice compared with that of the KPCi group (Figure 3H). The weight of BAT tissue was regained when implanting the pancreatic cancer cells into *Lcn2*-KO mice (Figure 3I). This is supported by H&E staining, which showed that the lipid droplets lost in KPCi mice were regained in KO^{*LCN2*}-KPCi animals (Figure 3J). Immunofluorescent staining against perilipin indicated the KPCi mice had smaller adipocytes. In contrast, the size of adipocytes in KO^{*LCN2*}-KPCi group were relatively larger (Figure 3K).

To explore the mechanism of thermogenesis improvement attained by *Lcn2* deletion, we further examined thermogenic and BAT signature

genes. BAT produces heat mainly through uncoupling protein 1 (*Ucp1*). The gene expression of *Ucp1* was reduced after tumor cell implantation in the WT mice ($p = 0.067$); however, this did not reach statistical significance. In contrast, deficiency of *Lcn2* significantly increased the level of *Ucp1* in the tumor-bearing mice ($p < 0.05$) (Figure 3L). Interestingly, the expression of *Adrb3* increased in the tumor bearing group of *Lcn2*-KO mice ($p < 0.05$) (Figure 3M). We also checked the brown development regulator gene *Prdm16* and did not see a difference (Figure 3N). In addition, the expression of *Lcn2* was increased by more than 15-fold in the KPCi mice compared with the WT mice (Figure 3O).

Together, these results suggest that the removal of inhibitory effect of *Lcn2* partially reversed hypothermia driven by end-stage cachexia by activating thermogenesis and improving BAT function.

3.4. Adipose tissue inflammation is reduced in *Lcn2* KO KPCi mice with improved systemic metabolic performance

Loss of iWAT in the KPCi mice and its reversal in the KO^{*LCN2*}-KPCi mice prompted us to investigate the inflammatory changes during tumor progression. Immunoblotting of iWAT from WT and KO^{*LCN2*} mice failed to detect *Lcn2* expression (Figure 4A). As expected, we were unable to detect *Lcn2* in KO^{*LCN2*}-KPCi mice (Figure 4B) confirming that the *Lcn2* detected in WT-KPCi group did not originate from the tumor. Furthermore, compared with iWAT from KO^{*LCN2*}-KPCi mice, the iWAT of WT-KPCi mice showed tissue shrinkage (Figure 4C) and decreased lipid droplet (Figure 4D). We noticed a substantial reduction of the lipolysis marker adipose triglyceride lipase (ATGL) in iWAT from *Lcn2*-KO mice in contrast with WT, indicating that *Lcn2* suppression reduces lipolysis (Figure 4E). In contrast, the expression of ATGL in the WT-KPCi mice showed a tendency to increase compared with WT (Supplementary Fig. 4A). Comparison of KO^{*LCN2*}-KPCi to the WT-KPCi mice revealed that ATGL expression was considerably lower in KO^{*LCN2*}-KPCi (Figure 4F), which explains that the increase of iWAT mass in KO^{*LCN2*}-KPCi mice was partly due to inhibition of lipolysis (Figure 3D–E).

Adipose tissue inflammation is a hallmark of pancreatic cancer cachexia. Therefore, we next examined inflammation in iWAT and the immune cell spectrum. Masson's trichrome staining revealed that adipose tissue fibrosis was markedly reduced in KO^{*LCN2*}-KPCi mice compared with KPCi mice (Figure 4G). Supporting this, we found a significant reduction in total immune cells (CD45+) in the iWAT of KO^{*LCN2*}-KPCi mice compared with KPCi mice ($p < 0.01$) (Figure 4H). The number of CD11b + F4/80+ cells in the KO^{*LCN2*}-KPCi group was also significantly lower compared with the KPCi mice ($p < 0.05$) (Supplementary Fig. 4B); however, there was no difference in the proportion of CD11b + cells (M1) and CD206+ cells (M2 macrophages) cells in the total macrophages (F4/80+CD11b) (Supplementary Figs. 4C–D). In contrast, we found that CD4+ cells were dramatically decreased in KO^{*LCN2*}-KPCi mice compared with WT-KPCi mice (Figure 4I), suggesting a lower level of active inflammation in adipose tissue of KO^{*LCN2*}-KPCi mice. These findings indicate that the deletion of *Lcn2* in KPCi mice improved adipose tissue functionality by minimizing both lipolysis and inflammation. However, the systemic response to the deletion of *Lcn2* in KPCi mice model is unknown.

We next evaluated the metabolic performance of groups using the Promethion metabolic cage system. We discovered that KO^{*LCN2*}-KPCi mice consumed significantly more oxygen than WT-KPCi mice ($p < 0.01$) (Figure 4J–K). Despite the higher fat mass (Figures 3D–E, 4C–D) observed in animals with *Lcn2* deletion, the rate of energy expenditure was significantly higher in the KO^{*LCN2*}-KPCi mice ($p < 0.05$) (Figure 4L–M). In contrast, when the animals were housed

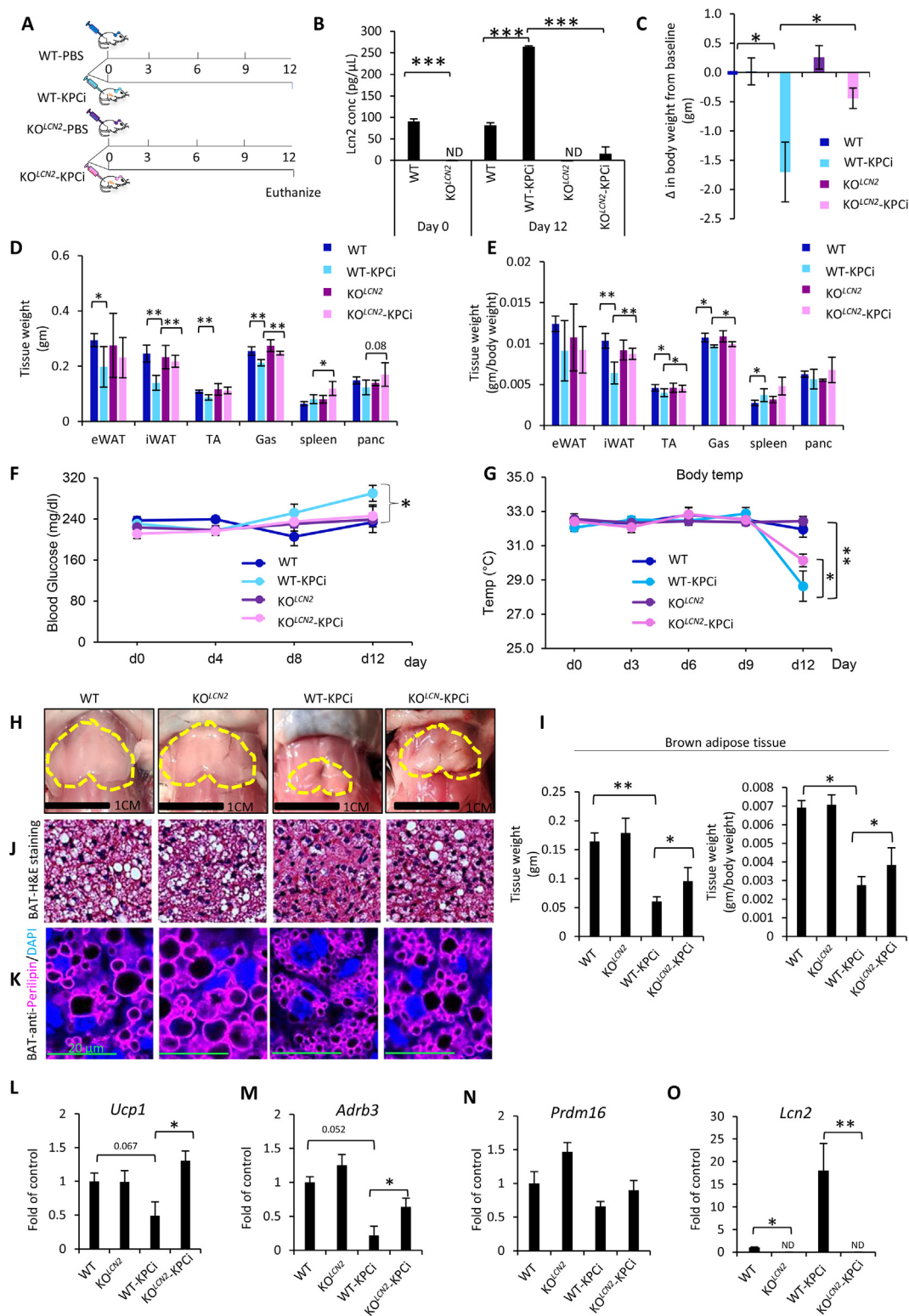


Figure 3: Reduced fat wasting and augmented normothermia in BAT of *Lcn2* deficient KPCi mice. **A**) Strategy for establishing the four experimental groups: KO^{Lcn2}-KPCi (*Lcn2* knockout mice implanted with KPC tumor cells), WT-KPCi (wild-type mice implanted with KPC tumor cells), KO^{Lcn2} (*Lcn2* KO mice administered with PBS) and WT (wild-type mice administered with PBS). **B**) Plasma *Lcn2* levels were analyzed by ELISA at day 0 and day 12 post PBS or KPC cell inoculation in mice. **C**) Change in body weight from the baseline (day 0 to day 12). **D, E**) Tissue weight (**D**) and tissue weight normalized by total body weight (**E**). **F**) Non-fasting blood glucose was measured at 10 am on the indicated days. **G**) Surface body temperature was measured at the indicated time points. **H**) Representative image of BAT (indicated by yellow dotted line). **I**) BAT weight in the indicated groups. **J**) Hematoxylin and eosin staining of BAT (white, lipid droplet; purple, nuclei; red, cytoplasm and extracellular matrix). **K**) Immunofluorescent staining of perlipin (purple; original red color changed to purple for clarity) and nuclei (DAPI, blue) in BAT. **L–O**) qRT-PCR of *Ucp1*, *Adrb3*, *Prdm16* and *Lcn2* in BAT. $n = 5$. **A–I**, $n = 5$. * $p < 0.05$, ** $p < 0.01$, *** $p < 0.001$.

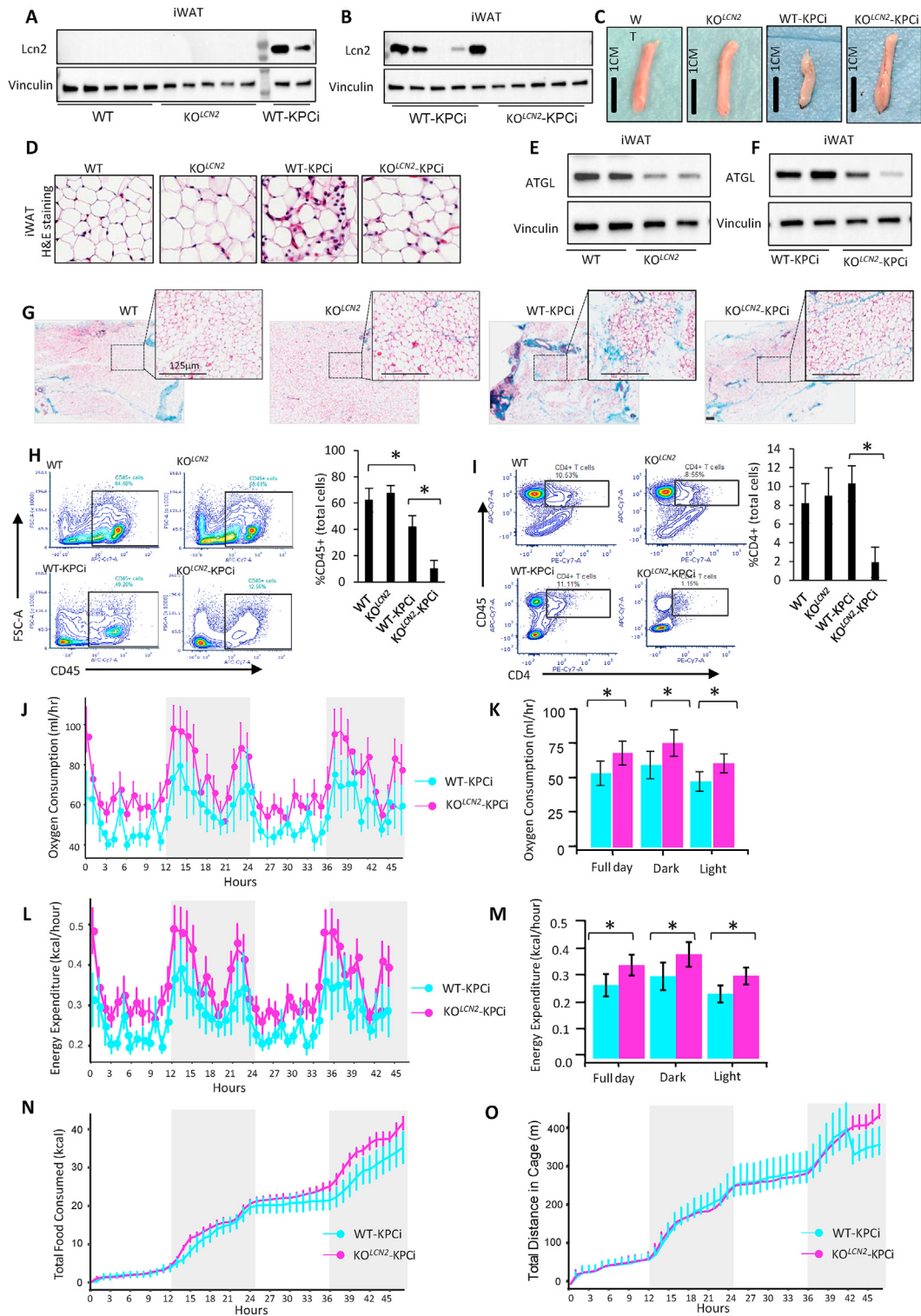


Figure 4: Adipose tissue inflammation was reduced in *Lcn2*-deficient pancreatic cancer mice. **A)** Immunoblot analysis of *Lcn2* protein in inguinal adipose tissues from WT and *Lcn2*-KO mice. Lysates from inguinal white adipose tissue (iWAT) of WT-KPCi mice used as positive control, n = 5. **B)** Immunoblot analysis of *Lcn2* in iWAT from WT and *Lcn2*-KO mice inoculated with KPC cells, n = 5. **C)** Representative image of iWAT, n = 5. **D)** Hematoxylin and eosin staining of iWAT, n = 3. **E, F)** Immunoblot analysis of ATGL (adipose triglyceride lipase) protein in inguinal adipose tissues, n = 5. **G)** Trichrome stained images of iWAT, n = 3. **H, I)** FACS analyses to identify immune cell populations gated out of total live cells isolated from iWAT tissue of indicated groups of mice. CD45⁺ cells (H) and CD4⁺ cells (I), n = 5. Representative images are shown, n = 5. **J, K)** Rate of oxygen consumption measured during light and dark cycle using the Promethion metabolic cage system (J) and quantitative analysis (K), n = 4–5. **L, M)** Rate of energy expenditure measured during light and dark cycle using the Promethion metabolic cage system (L) and quantitative analysis (M), n = 4–5. **N)** Total food consumption measured hourly for individually housed animals using Promethion metabolic cage system, n = 5. **O)** Total distance in cage measured hourly for individually housed animals using Promethion metabolic cage system, n = 5. *p < 0.05.

individually, hourly food intake showed a tendency of increase in the KO^{LCN2}-KPCi mice compared with the WT-KPCi (Figure 4N). However, this difference did not reach statistical significance and may be from the small number of mice. The KO^{LCN2}-KPCi mice exhibited improvement in the total distance in the cage only during the last 6 h (Figure 4O). These findings suggest that inhibiting Lcn2 during tumor progression increases metabolic output by reducing both adipose tissue inflammation and lipolysis.

3.5. Lcn2 KO KPCi mice exhibited reduced muscle atrophy during PDAC progression

Because of the fat wasting, hypothermia and muscle mass changes initiated by PDAC induced cachexia (Figure 3D–E), we investigated muscle atrophy in our mice model. The histologic examination of tibialis anterior muscle tissues (TA) by Masson's trichrome staining revealed that tissue fibrosis is markedly increased in tibialis anterior of WT-KPCi mice compared to WT mice (Figure 1A). This was further supported by significantly higher number of total immune cells (CD45+) in tibialis anterior of WT-KPCi mice compared to the control (Supplementary Fig. 5A). However, in Lcn2-deficient KPC mice this phenotype was partly resolved (Figure 5A). To validate this observation, we used the muscle atrophy molecular markers, muscle RING-finger protein-1 (MuRF-1) and muscle atrophy F-box gene (Fbx32). We found a substantial increase in MuRF-1 and Fbx32 levels in both the gastrocnemius and tibialis anterior in WT-KPCi mice compared with tumor-free mice (Figure 5C). Both proteins were markedly reduced in both the gastrocnemius and tibialis anterior of Lcn2 KO KPCi mice compared with WT-KPCi mice (Figure 5D). However, in the absence of the tumor we found no difference in MuRF-1 between WT and KO mice (Figure 5B). The increase in muscle atrophy markers can be partly explained by the increase level of Lcn2 during tumor progression. In addition, we examined the extent embryonic MyHC protein (MyHC3) expression in TA tissue. We observed slight increase in MyHC3 in Lcn2 KO KPCi mice compared with WT-KPCi mice (Figure 5E).

To verify the effect of PDAC-induced adipocyte-originated Lcn2 on skeletal muscle myogenesis, we isolated SV cells from iWAT of 10-week-old WT and KO^{LCN2} mice. The SV cells were then differentiated into mature white adipocytes. We then added CM from KPC cells to WT and Lcn2-KO primary adipocytes (Figure 5F). ELISA results showed that cancer-adipogenic media from WT adipocytes secreted considerably more Lcn2 than non-cancer conditioned media (Figure 5G). This result is consistent with our data *in vitro* (3T3-L1 adipocytes; Figure 1I) and *in vivo* (in mice after tumor cell implantation; Figure 2B). Strikingly, Lcn2 levels were unusually low in Lcn2-KO adipocytes treated with cancer medium (Figure 5G), confirming that the source of Lcn2 is from the adipocytes.

Next, we cultured C2C12 myoblasts with WT or Lcn2-ko adipogenic medium that was pre-treated by conditioned media from KPC cells. When C2C12 myoblasts treated with CM derived from Lcn2-ko adipocytes (pretreated with KPC cell CM), MyHC expression was partially restored, implicating that Lcn2 secreted from adipocytes stimulated by PDAC inhibit myotube development (Figure 5H–I). The *in vitro* model (Figure 5H) treated with conditioned media from primary adipocytes did not exhibit apoptosis as shown by absence of cleavage of caspase 3 and significantly lower level of lactate dehydrogenase (LDH) activity (Supplementary Figs. 5B–C).

4. DISCUSSION

The present study revealed three important findings. First, Lcn2 was identified as potent mediator of the crosstalk between adipose tissue

with muscle and tumor. Second, drastic hypothermia (<30 °C) caused by suppression of the thermogenesis pathway and fat loss accompanied by early immune cell infiltration in BAT during pancreatic cancer cachexia in mice. Third, inhibition of Lcn2 in pancreatic cancer mice alleviated hypothermia, in line with previous work by Olson et al. [45], and reduced adipose tissue and muscle atrophy. These findings suggest that Lcn2 disrupts communication between tissues through hypothermia-induced tumor progression (Figure 6A).

The 5-year overall survival rate of pancreatic cancer is 11% [3], and about 80% of patients develop cachexia [43]. Therefore, it is not surprising that KPCi mice exhibit aggressive tumor progression with weight loss, adipose tissue wasting and muscle atrophy, which is considered a hallmark of cancer cachexia. Other groups also reported that pancreatic cancer led to adipose tissue wasting [44,45].

In the current study, when 3T3-L1 adipocytes were treated with secretomes from PDAC cells (Figure 1A–C), FFA and glycerol levels increased with a substantial decrease in lipid droplets, indicating enhanced lipolysis. This coincides with a report showing loss of lipid droplets when adipocytes were co-cultured with breast cancer cells or treated with CM from KPC cells [46,47].

Here we showed that cancer cell-induced adipocytes secrete adipocytokines. Using a protein array, we identified Lcn2 as a potential mediator that is secreted by adipocytes in response to PDAC. This was supported by elevated Lcn2 levels both *in vitro* and *in vivo* (Figures 1I and 2B).

While Olson et al. used different mouse models, the authors also reported an increase in Lcn2 in the plasma of an orthotopically implanted KPC mouse model compared with sham controls. They observed no difference in Lcn2 protein levels in bone marrow between the sham and tumor models. However, the authors demonstrated significant production of Lcn2 within bone marrow compartment and neutrophils [45].

Neutrophil gelatinase-associated lipocalin (NGAL, lipocalin 2, Lcn2 or siderocalin) is a 178-amino acid, 25 kDa glycoprotein that was first purified and identified in 1993 by Kjeldsen et al. and found in human neutrophils in 1994 [48,49]. In 2007, Yan et al. reported that Lcn2 was highly expressed in WAT compared with other tissues such as the heart, brain, spleen, lung, liver, skeletal muscle, kidney, testis, and BAT [38]. Increasing evidence also suggests that Lcn2 is involved in inflammation and a biomarker for inflammatory and metabolic diseases [50].

By morphometric analysis of BAT, we observed a dramatic loss of fat content in BAT of KPCi mice. BAT is an essential organ for thermogenesis and maintenance of body temperature [39]. In line with this function, on day 12 after KPC cell inoculation, we observed a decrease in body temperature (hypothermia) in KPCi mice, which confirmed earlier findings [17]. We discovered immune cells (CD45+ and CD11c + F4/80+ cells) infiltrating BAT during the early stages of tumor development. However, at a later time point, this effect subsided. Our findings revealed that BAT dysfunction begins earlier as evidenced by lower body temperature in the later stages of tumor progression.

The association of BAT function with cancer progression is uncertain. Previous research found that when mice were housed in a cold environment (10 °C) after being inoculated subcutaneously with LLC cells, the development of metastatic lung nodes and tumor growth were accelerated [51]. In another study, hyperthermic (39–40 °C) mice had smaller tumors than hypothermic (34 °C) mice [52]. We explored whether the combination of hypothermia and tumor progression intensifies fat lipolysis, notably in BAT. Some studies showed that short-term hypothermia in rats raised FFA levels in the blood,

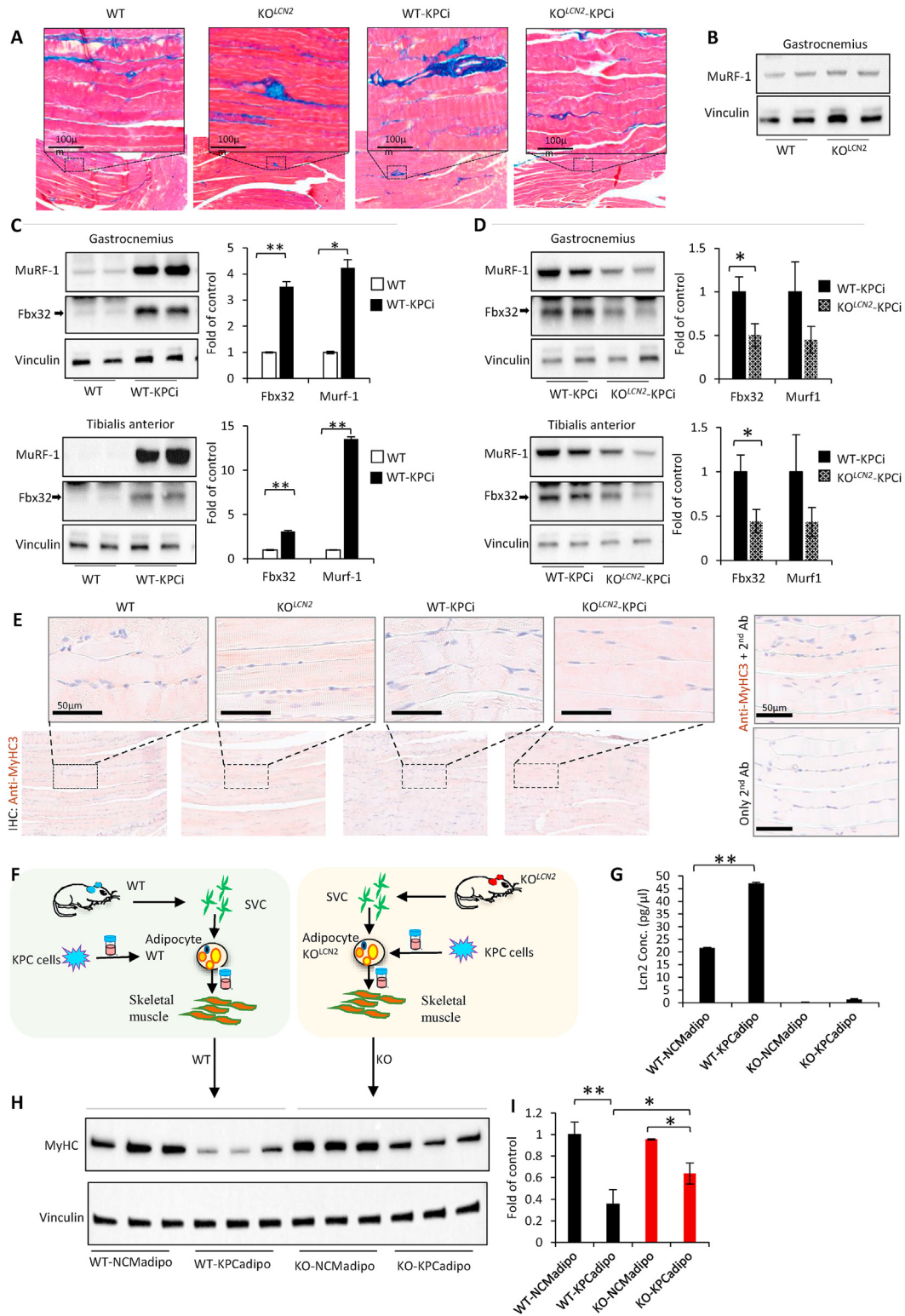


Figure 5: Reduced muscle wasting in *Lcn2* deficient KCPi mice and cancer induced adipogenic media from *Lcn2*-KO adipocytes improves myotube formation. **A)** Trichrome stained images of tibialis anterior; representative images are shown. **B)** Representatives immunoblot analysis of skeletal muscle atrophy markers MuRF-1. **C, D)** Representative immunoblot analysis and densitometry of band intensity of skeletal muscle atrophy molecular markers MuRF-1 and Fbx32 proteins. $n = 5$. **E)** Immunohistochemistry (IHC) staining of tibialis anterior (TA) tissues against MyHC3 protein. For the nuclei, hematoxylin counterstain was performed. Representative figures are shown, $n = 3$. The staining control with or without primary antibody (anti-MyHC3) is shown at right panel. **F)** Stromal vascular (SV) fractions isolation from iWAT of WT and *Lcn2*-KO mice differentiated to matured white adipocytes. The adipocytes were treated with conditioned media from cancer cells. Subsequently, cancer adipogenic media was collected and used to treat C2C12 cells. **G)** Lcn2 levels in cancer induced adipogenic media from primary matured white adipocytes measured by ELISA. $n = 4$. **H, I)** Immunoblot (G) and densitometric (H) analysis of MyHC in C2C12 after treatment with cancer cells induced adipogenic media. $n = 3$. * $p < 0.05$, ** $p < 0.01$.

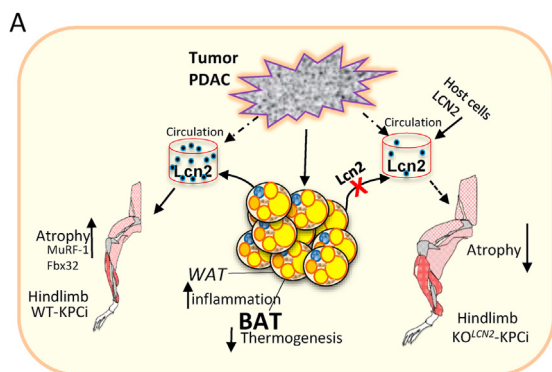


Figure 6: Schematic drawing showing role of Lcn2 as a communication factor between adipose tissue with muscle and tumor.

which is consistent with our finding, and this rise was associated with increased lipid-mobilizing activity [17,53]. Similarly, in older human patients with accidental hypothermia (core temperatures 25.0–35.5 °C), concentrations of non-esterified fatty acids, ketone bodies and glucose were high, indicating fat was used as the primary fuel at very low body temperatures. Although we observed hypothermia at a later stage, the primary mechanisms that initiate and promote lipolysis in adipocytes during cachexia are unclear [54]. This likely involves a complex signaling network interconnecting several organs and we propose that adipocyte secretomes play a major role in this process. We identified Lcn2 as a potential mediator secreted by adipocytes. Lcn2 deletion in mice was sufficient to attenuate loss of fat and muscle mass along with maintaining lower glucose level in the KPC model of cancer cachexia. Importantly, loss of total body weight was not entirely prevented in *Lcn2*-KO mice with KPC-induced cachexia despite preservation of fat and muscle mass. In agreement with our data, another study showed that Lcn2 was implicated as a link in the tumor microenvironment between obesity and inflammation during the progression of PDAC [37]. Although the importance of Lcn2 in the regulation of adipose tissue metabolism remains elusive [55,56], we show that *Lcn2* expression was dramatically increased in adipose tissue only in the presence of pancreatic cancer. However, Lcn2 was completely abolished in the KO mice with or without the presence of the tumor, indicating Lcn2 did not originate from the tumor. Interestingly, we found that ATGL expression was reduced in iWAT of the *Lcn2*-KO mice. ATGL and hormone sensitive lipase have been shown to increase in cancer patients along with elevated serum FFAs [57]. The breakdown of lipids into fatty acids is a crucial step in adipose wasting, and genetic ablation of ATGL prevents fat loss and preserves skeletal muscle mass in lung cancer-induced cachexia in mice [58]. We speculated the hypothermia instituted by the tumor was a driving factor of lipolysis observed in BAT. Therefore, to monitor hypothermia, we measured body temperature. The inhibition of *Lcn2* in KPCi mice using either anti-Lcn2 antibody neutralization or genomic ablation restored normothermia. This is supported by previous research showing that when WT and *Lcn2*-KO mice were exposed to a 4 °C environment, the *Lcn2*-KO mice had significantly higher body temperature. In contrast, *Lcn2* overexpression in WT-Tg mice led to markedly lower body temperature compared with control WT mice during cold treatment [62]. Noticeably, we observed an increase in lipid droplets in BAT of *Lcn2*-KO mice compared with WT mice when both groups harbored tumors, indicating a reduction in lipolysis. Our findings support a previous report which showed that rosiglitazone treatment for 25 days

increased Ucp1-mediated thermogenesis and energy expenditure in BAT of *Lcn2*^{-/-} mice compared with WT mice [59].

The mechanism by which Lcn2 inhibits BAT thermogenic activity is unknown. In the current study, the BAT of tumor-bearing mice exhibited a more than 15-fold increase in *Lcn2* gene expression (Figure 3O). In contrast, β 3-AR gene expression (*Adrb3*) was significantly reduced (Figure 3M). Studies have shown that β 3-AR stimulation increases intracellular cAMP levels through activation of adenylyl cyclase; cAMP then activates the PKA signaling cascades in adipocytes, which triggers lipolysis and thereby thermogenic gene expression [60]. In the current study, both *PKA* (*Prkaa1*) and *Plin1* were significantly downregulated after tumor cell inoculation (Figure 2L). In a study of a KPC engrafted mouse model, Michaelis et al. reported the shrinking of BAT and decreased *Ucp1* expression during the sick stage of tumor-bearing mice [17]. Zhang et al. also found a decrease in both tissue weight and Ucp1 expression in BAT of mice orthotopically inoculated with Panc02 cells compared with controls [61]. Consistent with these reports, we also observed a significant reduction in BAT mass and a tendency of decrease in expression of *Ucp1* in BAT of tumor-bearing mice. KEGG pathway enrichment analyses revealed a suppression of thermogenesis-related pathways such as PKA and PPAR signaling, oxidative phosphorylation and the TCA cycle in BAT in response to tumor cell inoculation. Inflammatory pathways, such as JAK-STAT and IL17 signaling pathways, were activated in BAT by the tumor (Figure 2J). Inhibition of Lcn2 increased β 3-AR and Ucp1 in BAT of tumor-bearing mice (Figure 3L–M). This indicates that the hypothermia we observed in the tumor-bearing mice might be partly from blockade of sympathetic β 3 activity in the BAT and suppression of BAT sensitivity to noradrenaline [62].

In tumor-bearing mice, Lcn2 deficiency significantly reduced fibrosis and decreased immune cell infiltration and active inflammation of adipose tissue, as evidenced by a decrease in CD45⁺ and CD4⁺ immune cells [63]. Interestingly, when Lcn2 was inhibited in KPCi mice, the rate of oxygen consumption and energy expenditure was significantly increased, indicating partial recovery of the metabolic deficit. Phenotypic changes in adipose tissue influence muscle function. In fact, a decrease in muscle mass is often observed in late stages of cachexia following fat loss in mouse models and in certain cancer patients [64]. The total number of CD45⁺ immune cells were significantly increased in the tibialis anterior muscles of KPCi mice and which is supported by increase in fibrosis. Previous reports showed that tumor burden affected the morphology of tibialis anterior and diaphragm muscles in orthotopic pancreatic cancer patient-derived xenograft mice [69]. In humans, compared to control subjects, skeletal muscle of PDAC patients showed increased collagen content which was positively correlated with body weight loss [70].

The most common muscle atrophy molecular markers MuRF-1 and Fbx32 were reduced in the gastrocnemius and tibialis anterior muscles of *Lcn2*-KO tumor bearing mice compared with WT mice. A tendency of muscle regeneration was observed in tibialis anterior tissue of *Lcn2*-KO tumor bearing mice compared with WT mice. This was supported further by our *in vitro* model. In C2C12 myoblasts treated with *Lcn2*-KO primary adipocyte secretome (pre-induced by pancreatic cancer cells CM), the expression of MyHC was markedly increased (Figure 5H–I) with significant increase in *Fbx32*. To support this observation, treatment of C2C12 by recombinant Lcn2 alone also reduced myotube formation, confirming the direct effect of Lcn2 on muscle. In a similar fashion, the neutralization of tumor-derived PTHrP prevented fat loss, thereby improving muscle mass and strength [65]. In this study, we did not observe significant difference in the total distance walk in the cage

by *Lcn2*-KO tumor bearing mice compared to control. Our mouse model develop tumor aggressively in 12 days. We propose further study such as treadmill exercise and grip strength using slow growth tumor model to evaluate the effect on muscle activity. Using orthotopic tumor model mice, Olson et al. reported an elevation in circulating Lcn2 levels is negatively correlated with food consumption and lean muscle mass. By using pair-feeding studies, the authors observed no difference in skeletal or cardiac tissue catabolism between *Lcn2*-KO and WT tumor-bearing mice indicating that the muscle-sparing effects of Lcn2 blockade are attributable to increased food intake alone [45]. Likewise, during the hourly caloric intake assessment for 48 h duration using a metabolic cage system, we observed that *Lcn2*-deleted KPCi mice consumed slightly more food than WT-KPCi mice. This difference did not reach statistical significance and may be from the small number of mice or model difference. However, whether Lcn2 affects BAT function through an appetite-regulating role remains unclear. Our study suggests that the hypothermia we observed during the late stage of tumor progression led to more energy wasting than energy produced.

This study has three major strengths. First, no research has been done on the role of Lcn2 in regulating brown fat depots and thus maintaining normothermia during pancreatic cancer cachexia. Hypothermia and fat loss in BAT were consistently observed during tumor progression in our models. Second, this study suggests that Lcn2 acts as a communication agent during adipose tissue—muscle-tumor crosstalk in pancreatic cancer. Third, the present study used multiple *in vitro* and *in vivo* models that reflect the common phenotypes of cancer-induced cachexia.

This study had some limitations. First, as a model for pancreatic cancer, we used heterotopic flank murine-derived cancer cell lines implanted into syngeneic mice. The inability to mimic the tumor microenvironment is a significant disadvantage of this model. Orthotopic tumor models may better represent the surrounding tumor environment; however, this model experiences surgical trauma. Second, although tumors grew quickly and reached the maximum size in 12 days, models aimed at producing slow-growing tumors are needed to investigate the mechanisms underlying cachexia early in the disease process. We are now establishing a tamoxifen-inducible pancreatic cancer model. Finally, our initial observations led us to concentrate on the impacts of Lcn2 produced by adipocytes. However, Lcn2 is also secreted by other cell types such as Olson et al. demonstrated Lcn2 produced by bone marrow compartment and neutrophils [45]. It is important to refine our findings using adipose tissue—specific *Lcn2*-KO mice. Furthermore, we propose additional mechanistic studies of BAT that may lead to therapeutic targets that prevent energy wasting during pancreatic cancer cachexia.

5. CONCLUSION

We and others demonstrated that loss of Lcn2 is beneficial in the preservation of fat and muscle mass during pancreatic cancer cachexia [45]. Other tumor-derived cachectic molecules with similar effects likely exist. New therapies that target these molecules and block fat thermogenesis have the potential to fight cachexia and hence improve patient survival.

ETHICS APPROVAL AND CONSENT TO PARTICIPATE

All experiments with mice were reviewed and approved by the City of Hope Institutional Animal Care and Use Committee (Protocol#20039).

CONSENT FOR PUBLICATION

Not applicable.

AVAILABILITY OF DATA AND MATERIALS

All data generated or analyzed during this study are included in this published article and its supplementary information files.

FUNDING

This research was supported by Genentech Royalty to KI, USA. Research reported in this publication included work performed in Pathology Core, the Integrative Genomics and Bioinformatics Core supported by the National Cancer Institute of the National Institutes of Health (NIH) under grant number P30CA033572, USA. The content is solely the responsibility of the authors and does not necessarily represent the official views of the NIH.

AUTHORS' CONTRIBUTIONS

M.L. and K.I. conceived and designed research; M.L., J.C., G.Z. and Y.T. performed experiments; M.L. and J.C. analyzed data; M.L., J.C., and K.I. interpreted results of experiments; M.L., and J.C. prepared figures; M.L. and K.I. drafted manuscript; J.C., Y.T., G.Z., T.Y., G.L., and K.I. discussed the results and critically revised the manuscript, M.L., G.L. and K.I. edited and revised manuscript. K.I. reviewed the manuscript and directed the work.

DATA AVAILABILITY

Data will be made available on request.

ACKNOWLEDGEMENTS

We thank A. Ehsani, PhD, C. Sun, PhD, J. Murray, PhD, Comprehensive Metabolic Phenotyping Core and the Central Research Laboratory of City of Hope National Medical Center for their technical assistance in this study. We thank Gabrielle White Wolf, PhD, from Edanz (www.edanz.com/ac) for editing a draft of this manuscript. A part of this study was presented at the 6th Cancer Cachexia Conference.

CONFLICT OF INTEREST

None. YT is an employee of Wakunaga Pharmaceutical Co., Ltd.

APPENDIX A. SUPPLEMENTARY DATA

Supplementary data to this article can be found online at <https://doi.org/10.1016/j.molmet.2022.101612>.

REFERENCES

- [1] Lim, S., Brown, J.L., Washington, T.A., Greene, N.P., 2020. Development and progression of cancer cachexia: perspectives from bench to bedside. *Sports Medicine and Health Science* 2:177–185.
- [2] Tan, C.R., Yaffee, P.M., Jamil, L.H., Lo, S.K., Nissen, N., Pandol, S.J., et al., 2014. Pancreatic cancer cachexia: a review of mechanisms and therapeutics. *Frontiers in Physiology* 5:88.
- [3] Society, A.C., 2022. *Cancer facts & figures*. American Cancer Society.

- [4] Henriques, F., Lopes, M.A., Franco, F.O., Knobl, P., Santos, K.B., Bueno, L.L., et al., 2018. Toll-like receptor-4 disruption suppresses adipose tissue remodeling and increases survival in cancer cachexia syndrome. *Scientific Reports* 8:1–14.
- [5] Castillo-Armengol, J., Fajas, L., Lopez-Mejia, I.C., 2019. Inter-organ communication: a gatekeeper for metabolic health. *EMBO Reports* 20:e47903.
- [6] Priest, C., Tontonoz, P., 2019. Inter-organ cross-talk in metabolic syndrome. *Nature Metabolism* 1:1177–1188.
- [7] Rupert, J.E., Narasimhan, A., Jengelle, D., Jiang, Y., Liu, J., Au, E., et al., 2021. Tumor-derived IL-6 and trans-signaling among tumor, fat, and muscle mediate pancreatic cancer cachexia. *Journal of Experimental Medicine* 218: e20190450.
- [8] Romero, A., Eckel, J., 2021. Organ crosstalk and the modulation of insulin signaling. *Cells* 10:2082.
- [9] Rogal, J., Binder, C., Kromidas, E., Roos, J., Probst, C., Schneider, S., et al., 2020. WAT-on-a-chip integrating human mature white adipocytes for mechanistic research and pharmaceutical applications. *Scientific Reports* 10:1–12.
- [10] Nieman, K.M., Romero, I.L., Van Houten, B., Lengyel, E., 2013. Adipose tissue and adipocytes support tumorigenesis and metastasis. *Biochimica et Biophysica Acta* 1831:1533–1541.
- [11] Fonseca, G., Farkas, J., Dora, E., von Haehling, S., Lainscak, M., 2020. Cancer cachexia and related metabolic dysfunction. *International Journal of Molecular Sciences* 21:2321.
- [12] Fukawa, T., Yan-Jiang, B.C., Min-Wen, J.C., Jun-Hao, E.T., Huang, D., Qian, C.N., et al., 2016. Excessive fatty acid oxidation induces muscle atrophy in cancer cachexia. *Nature Medicine* 22:666–671.
- [13] Petruzzelli, M., Wagner, E.F., 2016. Mechanisms of metabolic dysfunction in cancer-associated cachexia. *Genes & Development* 30:489–501.
- [14] Paal, P., Pasquier, M., Darocha, T., Lechner, R., Kosinski, S., Wallner, B., et al., 2022. Accidental hypothermia: 2021 update. *International Journal of Environmental Research and Public Health* 19:501.
- [15] Stoner, H.B., Little, R.A., Frayn, K.N., 1983. Fat metabolism in elderly patients with severe hypothermia. *Quarterly Journal of Experimental Physiology (Cambridge, England)* 68:701–707.
- [16] Flo, T.H., Smith, K.D., Sato, S., Rodriguez, D.J., Holmes, M.A., Strong, R.K., et al., 2004. Lipocalin 2 mediates an innate immune response to bacterial infection by sequestering iron. *Nature* 432:917–921.
- [17] Michaelis, K.A., Zhu, X., Burfeind, K.G., Krasnow, S.M., Levasseur, P.R., Morgan, T.K., et al., 2017. Establishment and characterization of a novel murine model of pancreatic cancer cachexia. *Journal of Cachexia, Sarcopenia and Muscle* 8:824–838.
- [18] Pazos, P., Lima, L., Tovar, S., González-Touceda, D., Diéguez, C., García, M.C., 2015. Divergent responses to thermogenic stimuli in BAT and subcutaneous adipose tissue from interleukin 18 and interleukin 18 receptor 1-deficient mice. *Scientific Reports* 5:1–14.
- [19] Kawakami, Y., Sielski, R., Kawakami, T., 2018. Mouse body temperature measurement using infrared thermometer during passive systemic anaphylaxis and food allergy evaluation. *Journal of Visualized Experiments: JoVE*, 58391.
- [20] Fritz, J.M., Tennis, M.A., Orlicky, D.J., Lin, H., Ju, C., Redente, E.F., et al., 2014. Depletion of tumor-associated macrophages slows the growth of chemically induced mouse lung adenocarcinomas. *Frontiers in Immunology* 5: 587.
- [21] Lemecha, M., Morino, K., Imamura, T., Iwasaki, H., Ohashi, N., Ida, S., et al., 2018. miR-494-3p regulates mitochondrial biogenesis and thermogenesis through PGC1- α signalling in beige adipocytes. *Scientific Reports* 8:1–14.
- [22] Kato, M., Abdollahi, M., Tunduguru, R., Tsark, W., Chen, Z., Wu, X., et al., 2021. miR-379 deletion ameliorates features of diabetic kidney disease by enhancing adaptive mitophagy via FIS1. *Communications Biology* 4:1–17.
- [23] Mina, A.I., LeClair, R.A., LeClair, K.B., Cohen, D.E., Lantier, L., Banks, A.S., 2018. CalR: a web-based analysis tool for indirect calorimetry experiments. *Cell Metabolism* 28:656–666.e1.
- [24] Yamamoto, H., Morino, K., Mengistu, L., Ishibashi, T., Kiriya, K., Ikami, T., et al., 2016. Amla enhances mitochondrial spare respiratory capacity by increasing mitochondrial biogenesis and antioxidant systems in a murine skeletal muscle cell line. *Oxidative Medicine and Cellular Longevity*, 1735841.
- [25] Okazaki, Y., Murray, J., Ehsani, A., Clark, J., Whitson, R.H., Hirose, L., et al., 2020. Increased glucose metabolism in Arid5b-/- skeletal muscle is associated with the down-regulation of TBC1 domain family member 1 (TBC1D1). *Biological Research* 53:1–14.
- [26] Bolger, A.M., Lohse, M., Usadel, B., 2014. Trimmomatic: a flexible trimmer for Illumina sequence data. *Bioinformatics (Oxford, England)* 30:2114–2120.
- [27] Chen, S., Zhou, Y., Chen, Y., Gu, J., 2018. fastp: an ultra-fast all-in-one FASTQ preprocessor. *Bioinformatics (Oxford, England)* 34:i884–i890.
- [28] Dobin, A., Davis, C.A., Schlesinger, F., Drenkow, J., Zaleski, C., Jha, S., et al., 2013. STAR: ultrafast universal RNA-seq aligner. *Bioinformatics (Oxford, England)* 29:15–21.
- [29] Liao, Y., Smyth, G.K., Shi, W., 2019. The R package Rsubread is easier, faster, cheaper and better for alignment and quantification of RNA sequencing reads. *Nucleic Acids Research* 47:e47.
- [30] Robinson, M.D., McCarthy, D.J., Smyth, G.K., 2010. edgeR: a Bioconductor package for differential expression analysis of digital gene expression data. *Bioinformatics (Oxford, England)* 26:139–140.
- [31] de Hoon, M.J., Imoto, S., Nolan, J., Miyano, S., 2004. Open source clustering software. *Bioinformatics* 20:1453–1454.
- [32] Kim, S.Y., Volsky, D.J., 2005. PAGE: parametric analysis of gene set enrichment. *BMC Bioinformatics* 6:1–12.
- [33] Ge, S.X., Son, E.W., Yao, R., 2018. iDEP: an integrated web application for differential expression and pathway analysis of RNA-Seq data. *BMC Bioinformatics* 19:534.
- [34] Kanehisa, M., Furumichi, M., Sato, Y., Ishiguro-Watanabe, M., Tanabe, M., 2021. KEGG: integrating viruses and cellular organisms. *Nucleic Acids Research* 49:D545–D551.
- [35] Luo, W., Brouwer, C., 2013. Pathview: an R/Bioconductor package for pathway-based data integration and visualization. *Bioinformatics* 29:1830–1831.
- [36] Ge, S.X., Jung, D., Yao, R., 2020. ShinyGO: a graphical gene-set enrichment tool for animals and plants. *Bioinformatics (Oxford, England)* 36:2628–2629.
- [37] Gomez-Chou, S.B., Swidnicka-Siergiejko, A.K., Badi, N., Chavez-Tomar, M., Lesinski, G.B., Bekaii-Saab, T., et al., 2017. Lipocalin-2 promotes pancreatic ductal adenocarcinoma by regulating inflammation in the tumor microenvironment. *Cancer Research* 77:2467–2660.
- [38] Yan, Q.W., Yang, Q., Mody, N., Graham, T.E., Hsu, C.H., Xu, Z., et al., 2007. The adipokine lipocalin 2 is regulated by obesity and promotes insulin resistance. *Diabetes* 56:2533–2540.
- [39] Cannon, B., Nedergaard, J., 2004. Brown adipose tissue: function and physiological significance. *Physiological Reviews* 84:277–359.
- [40] Kajimura, S., Saito, M., 2014. A new era in brown adipose tissue biology: molecular control of brown fat development and energy homeostasis. *Annual Review of Physiology* 76:225–249.
- [41] Tsubota, A., Okamoto-Ogura, Y., Bariuan, J.V., Mae, J., Matsuoka, S., Nio-Kobayashi, J., et al., 2019. Role of brown adipose tissue in body temperature control during the early postnatal period in Syrian hamsters and mice. *Journal of Veterinary Medical Science* 81:1461–1467.
- [42] Xu, Z., You, W., Zhou, Y., Chen, W., Wang, Y., Shan, T., 2019. Cold-induced lipid dynamics and transcriptional programs in white adipose tissue. *BMC Biology* 17:1–21.
- [43] Fearon, K.C., Voss, A.C., Hustead, D.S., Group, C.C., 2006b. Definition of cancer cachexia: effect of weight loss, reduced food intake, and systemic

- inflammation on functional status and prognosis. *American Journal of Clinical Nutrition* 83:1345–1350.
- [44] Danaei, L.V., Babic, A., Rosenthal, M.H., Dennstedt, E.A., Muir, A., Lien, E.C., et al., 2018. Altered exocrine function can drive adipose wasting in early pancreatic cancer. *Nature* 558:600–604.
- [45] Olson, B., Zhu, X., Norgard, M.A., Levasseur, P.R., Butler, J.T., Buenafe, A., et al., 2021. Lipocalin 2 mediates appetite suppression during pancreatic cancer cachexia. *Nature Communications* 12:1–15.
- [46] Wang, Y.Y., Attané, C., Milhas, D., Dirat, B., Dauvillier, S., Guérard, A., et al., 2017. Mammary adipocytes stimulate breast cancer invasion through metabolic remodeling of tumor cells. *JCI Insight* 2:e87489.
- [47] Rupert, J.E., Narasimhan, A., Jengellej, D., Jiang, Y., Liu, J., Au, E., et al., 2021. Tumor-derived IL-6 and trans-signaling and crosstalk among tumor, muscle and fat mediate pancreatic cancer cachexia, vol. 2 e20190450.
- [48] Kjeldsen, L., Johnsen, A.H., Sengeløv, H., Borregaard, N., 1993. Isolation and primary structure of NGAL, a novel protein associated with human neutrophil gelatinase. *Journal of Biological Chemistry* 268:10425–10432.
- [49] Kjeldsen, L., Bainton, D.F., Sengeløv, H., Borregaard, N., 1994. Identification of neutrophil gelatinase-associated lipocalin as a novel matrix protein of specific granules in human neutrophils. *Blood* 83:799–807.
- [50] Abella, V., Scotece, M., Conde, J., Gómez, R., Lois, A., Pino, J., et al., 2015. The potential of lipocalin-2/NGAL as biomarker for inflammatory and metabolic diseases. *Biomarkers: Biochemical Indicators of Exposure, Response, and Susceptibility to Chemicals* 20:565–571.
- [51] Du, G., Zhao, B., Zhang, Y., Sun, T., Liu, W., Li, J., et al., 2013. Hypothermia activates adipose tissue to promote malignant lung cancer progression. *PLoS One* 8:e72044.
- [52] Du, G., Liu, Y., Li, J., Liu, W., Wang, Y., Li, H., 2013. Hypothermic microenvironment plays a key role in tumor immune subversion. *International Immunopharmacology* 17:245–253.
- [53] Gryczka-Dziadecka, A., 1983. Effect of hypothermia on lipolytic processes in blood and adipose tissue of rat. *Acta Physiologica Polonica* 34:457–465.
- [54] Rydén, M., Arner, P., 2007. Fat loss in cachexia—is there a role for adipocyte lipolysis? *Clinical Nutrition (Edinburgh, Scotland)* 26:1–6.
- [55] Guo, H., Jin, D., Zhang, Y., Wright, W., Bazuine, M., Brockman, D.A., et al., 2010. Lipocalin-2 deficiency impairs thermogenesis and potentiates diet-induced insulin resistance in mice. *Diabetes* 59:1376–1385.
- [56] Law, I.K., Xu, A., Lam, K.S., Berger, T., Mak, T.W., Vanhoutte, P.M., et al., 2010. Lipocalin-2 deficiency attenuates insulin resistance associated with aging and obesity. *Diabetes* 59:872–882.
- [57] Thompson, M.P., Cooper, S.T., Parry, B.R., Tuckey, J.A., 1993. Increased expression of the mRNA for hormone-sensitive lipase in adipose tissue of cancer patients. *Biochimica et Biophysica Acta* 1180:236–242.
- [58] Das, S.K., Eder, S., Schauer, S., Diwojky, C., Temmel, H., Guertl, B., et al., 2011. Adipose triglyceride lipase contributes to cancer-associated cachexia. *Science* 333:233–238.
- [59] D Jin, D., Guo, H., Bu, S.Y., Zhang, Y., Hannaford, J., Mashek, D.G., et al., 2011. Lipocalin 2 is a selective modulator of peroxisome proliferator-activated receptor-gamma activation and function in lipid homeostasis and energy expenditure. *FASEB Journal: Official Publication of the Federation of American Societies for Experimental Biology* 25:754–764.
- [60] Lowell, B.B., Flier, J.S., 1997. Brown adipose tissue, beta 3-adrenergic receptors, and obesity. *Annual Review of Medicine* 48:307–316.
- [61] Zhang, Y., Hu, S., Shangquan, J., Pan, L., Zhou, X., Yaghamai, V., et al., 2019. MRI assessment of associations between brown adipose tissue and cachexia in murine pancreatic ductal adenocarcinoma. *Internal Medicine: Open Access* 9:301.
- [62] Ishii, A., Katsuura, G., Imamaki, H., Kimura, H., Mori, K.P., Kuwabara, T., et al., 2017. Obesity-promoting and anti-thermogenic effects of neutrophil gelatinase-associated lipocalin in mice. *Scientific Reports* 7:15501.
- [63] Morris, D.L., Cho, K.W., Delproposto, J.L., Oatmen, K.E., Geletka, L.M., Martinez-Santibanez, G., et al., 2013. Adipose tissue macrophages function as antigen-presenting cells and regulate adipose tissue CD4+ T cells in mice. *Diabetes* 62:2762–2772.
- [64] Fouladiun, M., Körner, U., Bosaeus, I., Daneryd, P., Hylander, A., Lundholm, K.G., 2005. Body composition and time course changes in regional distribution of fat and lean tissue in unselected cancer patients on palliative care—correlations with food intake, metabolism, exercise capacity, and hormones. *Cancer* 103:2189–2198.
- [65] Kir, S., White, J.P., Kleiner, S., Kazak, L., Cohen, P., Baracos, V.E., et al., 2014. Tumour-derived PTH-related protein triggers adipose tissue browning and cancer cachexia. *Nature* 513:100–104.
- [66] Kanehisa, M., Goto, S., 2000. KEGG: Kyoto Encyclopedia of genes and genomes. *Nucleic Acids Research* 28:27–30.
- [67] Bajaj, P., Reddy Jr., B., Millet, L., Wei, C., Zorlutuna, P., Bao, G., et al., 2011. Patterning the differentiation of C2C12 skeletal myoblasts. *Integrative Biology (Camb)* 3(9):897–909.
- [68] Murphy, D.P., Nicholson, T., Jones, S.W., O’Leary, M.F., 2019. MyoCount: a software tool for the automated quantification of myotube surface area and nuclear fusion index. *Wellcome Open Research* 4.
- [69] Nosacka, R.L., Delitto, A.E., Delitto, D., Patel, R., Judge, S.M., Trevino, J.G., et al., 2020. Distinct cachexia profiles in response to human pancreatic tumours in mouse limb and respiratory muscle. *Journal of Cachexia, Sarcopenia and Muscle* 11(3):820–837.
- [70] Judge, S.M., Nosacka, R.L., Delitto, D., Gerber, M.H., Cameron, M.E., Trevino, J.G., et al., 2018. Skeletal muscle fibrosis in pancreatic cancer patients with respect to survival. *JNCI Cancer Spectrum* 2(3):pk043.